Mon. Not. R. Astron. Soc. **000**, 000–000 (0000) Printed 3 June 2005 (MN LATEX style file v2.2)

A detailed study of G35.2–0.7N: collimated outflows in a cluster of high-mass young stellar objects

A.G. Gibb[1,2⋆], M.G. Hoare[2], L.T. Little[3] and M.C.H. Wright[4]
[1]*Department of Astronomy, University of Maryland, College Park, MD 20742, USA.*
[2]*Department of Physics and Astronomy, University of Leeds, Leeds, West Yorkshire, LS2 9JT, UK.*
[3]*Electronic Engineering Laboratory, University of Kent at Canterbury, Kent, CT2 7NT, UK.*
[4]*Radio Astronomy Laboratory, Department of Astronomy, University of California, 601 Campbell Hall, Berkeley, CA 94720, USA.*

3 June 2005

ABSTRACT

We present a series of JCMT, BIMA and VLA observations of the massive star-forming region associated with G35.2–0.7N. These new observations shed considerable light on the nature of the outflows in this region. The combination of our CO, SiO and radio data suggest that there are perhaps as many as four outflows emanating from the core containing G35.2–0.7N.

CO J=3→2 maps show that the outflow has a curved appearance consistent with precession of a central driving source. However, the geometric centre of the flow is found to be not coincident with the radio jet source G35.2N but is instead closer to a peak in SiO, $H^{13}CO^+$ and dust continuum found in the BIMA data. An elongated finger of CO emission is detected to the north of centre which points back towards the radio jet centred on G35.2N, further ruling it out as the driving source of the larger-scale CO flow.

BIMA observations of the 3.5-mm continuum (which is dominated by dust), $H^{13}CN$ and $H^{13}CO^+$ emission trace a dense, elongated, rotating envelope with properties in good agreement with values derived from previous ammonia observations. The peak of the dust continuum and the $H^{13}CO^+$ peak a few arcsec to the south of G35.2N. SiO J=2→1 data delineate a well-collimated feature parallel with the axis of the CO outflow, but offset to the north by ∼10 arcsec. $H^{13}CO^+$ emission is detected at the possible origin of this flow but no radio source is observed.

VLA A-configuration observations at 6- and 3.5 cm resolve the radio jet into at least six discrete components, with positions consistent with previous observations. The central driving source, G35.2N, is only detected at 3.5 cm. At least two other sources are detected, one of which lies within the flattened core and may be associated with another flow inferred from recent L'-band observations. No radio source is detected at the geometric centre of the CO outflow.

Key words: ISM: clouds – ISM: individual: G35.2–0.7N – ISM: jets and outflows – radio lines: ISM – H II regions

1 INTRODUCTION

Outflows from low mass young stellar objects (YSOs) have been extensively studied, especially with the advent of sensitive, high-resolution millimetre facilities. A number of spectacular CO outflows have been mapped (e.g. Gueth & Guilloteau 1999, Lee et al. 2000) and the current consensus is that these outflows are driven by highly collimated jets, which are sometimes seen optically or in the emission of shock-excited H_2 or shock-ionized gas via radio continuum (Eislöffel 1997; Rodríguez 1997). The CO traces the gas swept up by the outflow as it ploughs into the surrounding cloud and effectively provides a time-integrated historical view of the flow evolution. The H_2 emission arises from within the shocked regions of the jet and provides an instantaneous view of the current interaction regions, as its cooling time is of order a year or so (Hollenbach & McKee 1979).

The study of outflows from high-mass YSOs is more problematic than for low mass sources for several reasons. Massive stars form in dense clusters and even the nearest massive YSOs lie at greater distances than typical low-mass star forming cores, both of which mean that confusion makes it difficult to correctly interpret observations of massive star forming regions. The contraction timescales of high-mass stars are short and their smaller numbers further renders the study of outflows from luminous YSOs challenging. For example, it is not clear whether high mass outflows are driven by collimated jets as evidence for their existence is scant. At

⋆ Email: agg@astro.umd.edu

present there appears to be only a few examples of luminous YSOs with well-defined jets such as HH80/81 (Martí et al. 1993), Cep A2 (Torrelles et al. 1996) and W3-H_2O (Wilner, Reid & Menten 1999). A recent survey of outflows form massive YSOs by Beuther et al. (2002) found a higher degree of collimation than previously observed. However, the majority of massive YSOs do not show evidence for jets.

Surprisingly some massive YSOs (notably S106 and S140-IRS1) actually appear to have winds which extend in the equatorial direction (Hoare 2002; Hoare et al. 1994). The radio emission from massive YSOs of ZAMS type B0 and later tends to be dominated by free-free emission from an ionized stellar wind rather than an H II region. Free-free emission from a stellar wind has a spectral index of +0.6 (Wright & Barlow 1974), compared with +2 (–0.1) for an optically thick (thin) H II region. The spectral index of a stellar wind may steepen to $\sim$1 or higher if the wind recombines at a finite distance from the star (Simon et al. 1983). An accelerated wind may also result in a spectral index greater than 0.6 (Panagia & Felli 1975).

The target for this present study is G35.2–0.7N, a massive star-forming region in which a jet-like radio structure is seen. G35.2–0.7N is associated with the IRAS source 18556+0136 (and hereafter will be referred to as G35.2N) lies approximately 2 kpc distant. Dent et al. (1985) derive a spectral class of B0.5 for the exciting star of the bipolar reflection nebula, corresponding to a luminosity of approximately 10^4 $L_\odot$ and a stellar mass of $\sim$15 $M_\odot$ (Allen 1973). A rotating interstellar-scale disc or toroid was detected in ammonia emission (Little et al. 1985) while a bipolar CO outflow was discovered to lie almost perpendicular to this disc (Dent et al. 1985). Heaton & Little (1988, hereafter HL88) made VLA observations of the radio emission at the centre of the outflow and revealed an elongated source orientated north-south, a position angle very different from that of the CO flow. HL88 resolved three main radio components arranged in a co-linear fashion labelled N, C and S. The centre component (C) is coincident with a cluster of OH masers (Brebner et al. 1987) and has a spectral index of 0.8, indicating a stellar wind (Wright & Barlow 1974), while the others have spectral indices close to zero, suggesting optically thin HII regions. The symmetry of the radio emission suggests a jet but the spectral indices are consistent with a number of embedded YSOs.

Also orientated north-south in G35.2N is a bipolar reflection nebula (the brightest part of which had previously been called G35.2N-IRS1), studied in detail by Walther, Aspin & McLean (1990). These authors speculated that a source G35N-star located in a region of high extinction was responsible for the nebula. The location of this proposed source is approximately 3 arcsec south of the radio source G35.2N. More recent L'-band infrared observations by Fuller, Zijlstra & Williams (2001) showed that the reflection nebula is still visible at L'-band, although its appearance supports the idea of a north-south jet emerging from G35.2N.

HL88 proposed that the large difference in position angle between the CO and radio was due to precession of a collimated, ionized jet, an interpretation given further support by Little, Kelly & Murphy (1998). These authors observed that high-velocity neutral atomic carbon was confined to a region with an intermediate position angle, indicating perhaps that ultraviolet radiation from the central star has penetrated into a cavity swept clear by the outflow (seen as the infrared reflection nebula), dissociating CO molecules on the near side of the shell. G35.2N is not alone in showing evidence for precession. The jet in HH80–81 is probably precessing, albeit through a much smaller angle (Martí et al. 1993), while Shepherd et al. (2000) invoke precession to explain the large angular offset between the large- and small-scale outflows in IRAS 20126+4104.

To explore further the precession hypothesis for G35.2N and determine the nature of the radio sources, we have carried out a detailed observational study of this outflow source in which we have mapped the outflow and disc in a variety of molecular tracers with the JCMT and BIMA as well as carried out high-resolution VLA observations of the jet itself. In the following sections we describe our observations and ultimately arrive at a new picture for the region containing G35.2N.

2 OBSERVATIONS

Observations were made at the 15-m James Clerk Maxwell Telescope (JCMT), Mauna Kea, Hawaii, the Berkeley-Illinois-Maryland Association (BIMA) array of nine (now ten) 6.1-m telescopes at Hat Creek, California, and the NRAO Very Large Array (VLA), New Mexico. From previous observations (e.g. Little et al. 1985) the systemic velocity is +34 km s^{-1} with respect to the local standard of rest (LSR).

The JCMT observations were carried out on the nights of 1995 April 16 ($C^{17}O$ only) and 1997 April 17 to 20 and made use of the common user receivers A2 (covering 200 to 280 GHz), B3i (300 to 380 GHz), B3 (315 to 370 GHz) and C2 (450 to 500 GHz). In the 1995 run, the weather was excellent with 225-GHz optical depths of $<$0.07. G34.3+0.2 and AFGL2591 were used as pointing sources (good to within 2 arcsec), and G34.3+0.2 was used as a secondary calibrator on which we obtained standard spectra. In this run, receiver B3i was used (double sideband) which had a system temperature of around 750 K, with the digital autocorrelation spectrometer (DAS) set to a bandwidth of 500 MHz (giving a spectral resolution of 378 kHz). The calibration uncertainty is estimated at 10 per cent. The (0,0) position in the JCMT maps is at RA(J2000) = $18^{\rm h}58^{\rm m}13.00^{\rm s}$, Dec(J2000) = $+01^\circ40'36.2''$

In the 1997 run the weather conditions were reasonably good (the optical depth at 225 GHz was typically 0.12) with pointing errors at $\sim$2 arcsec or less. Mars and G34.3+0.2 were used as pointing sources, with G34.3+0.2 used as a secondary calibrator. The instrumental setup employed the facility receivers A2, B3 (in both single- and double-sideband operation) and C2 in conjunction with the DAS as backend in the same configuration as above. Typical system temperatures were 380 K (A2), 600–1500 K (B3) and 3500 K (C2). Integration times were typically 5 to 10 minutes per point depending on system temperature and receiver. The calibration uncertainty is estimated at 10–20 per cent, again depending on receiver (with the smaller uncertainty corresponding to lower frequency data). Linear baselines were removed from all JCMT spectra. The target species were CO, ^{13}CO and $C^{17}O$ J=3$\rightarrow$2 (Rx B3) and SiO J=5$\rightarrow$4 (A2). The full-width-at-half-maximum (FWHM) diameter of the JCMT beam is 22 arcsec at 217 GHz (for the SiO 5$\rightarrow$4 line), 15 arcsec at 345 GHz (3$\rightarrow$2 CO, ^{13}CO and $C^{17}O$) and 10 arcsec at 461 GHz (CO 4$\rightarrow$3). All JCMT brightness temperatures are quoted in the text as $T_{\rm R}^*$ assuming a value for the forward scattering and spillover efficiency ($\eta_{\rm fss}$) of 0.8, 0.7 and 0.7 at each of the three frequencies given above.

The BIMA observations were carried out in a single track (with 5 hours on source) on 1997 April 18 with the array in its C configuration. The flux calibrator was 3C273 (assuming a flux density at 86 GHz of 32 Jy). The phase calibrator was 1751+096 (J2000) and was observed every 30 minutes. A flux density of 4.3 Jy was derived for 1751+096, bootstrapped from the flux density

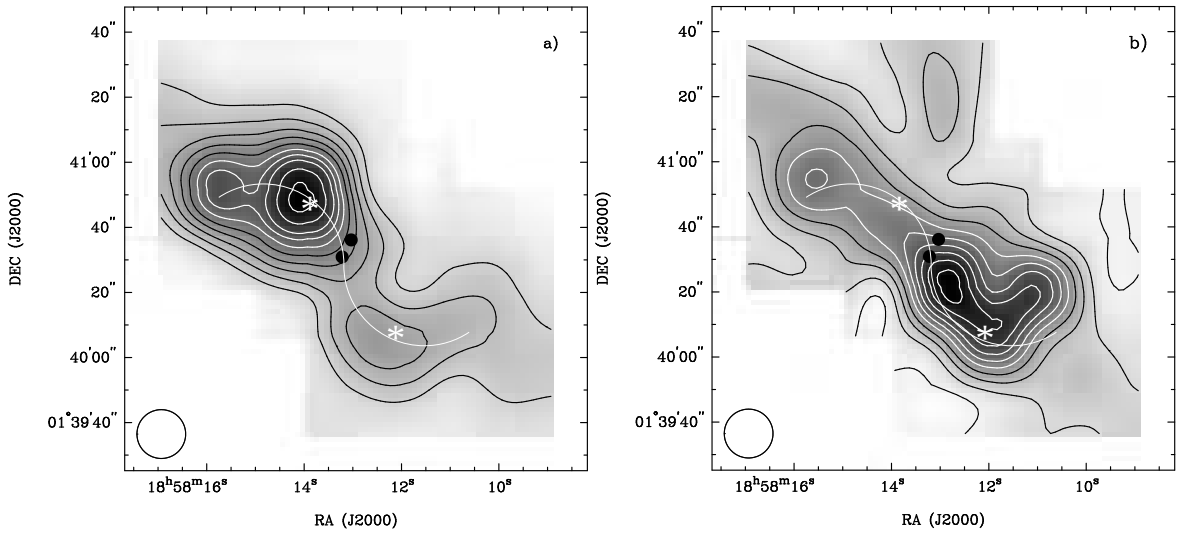

Figure 1. CO J=3→2 emission integrated between a) 5 and 30 km s^{-1} and b) 40 and 55 km s^{-1}. The redshifted emission is only half as bright as the blueshifted lobe (partly due to its smaller velocity coverage). The contours start at 25 (20) K km s^{-1}, increasing in steps of 25 (10) K km s^{-1}for the blueshifted (redshifted) emission. The greyscale is linear between 0 and 250 K km s^{-1} (blue) and 0 and 110 K km s^{-1} (red). The radio source G35.2N at (0,0) and millimetre source G35MM2 at (2.8,–5.2) arcsec offset are each marked with filled circle. The position of G35MM2 is taken from J.M. Carpenter (private communication). The white curve marks an 'S' shape which might be expected for a precessing source. The asterisks mark the positions 'B' and 'R' referred to in the spectra displayed in Fig. 2. The large open circle represents the 15-arcsec JCMT beam.

of 3C273. The instrumental setup permitted simultaneous observation of the SiO J=2→1, H^{13}CO$^+$ J=1→0 and the hyperfine triplet of H^{13}CN J=1→0, F=1→1, 2→1 and 1→0 lines with a bandwidth and spectral resolution of 25 MHz and 98 kHz (0.34 km s^{-1}) respectively. In addition a continuum band of 100 MHz was observed which was used to construct the 3.5-mm continuum image. Line-free channels were averaged and subtracted from the line data before images were made. Data calibration and reduction was performed using standard procedures within MIRIAD. The size of the restoring CLEAN beam was 10×8 arcsec^2 (uniform weighting), rising to 11×9 arcsec^2 for natural weighting. Most images were formed with natural weighting to maximize sensitivity. The pointing centre for the BIMA observations is at RA(J2000) = 18$^{\rm h}$58$^{\rm m}$13.13$^{\rm s}$, Dec(J2000) = +01°40′39.50″.

The VLA observations were carried out on 1999 September 15 in the A configuration. G35.2N was observed at C, X and U bands with a total bandwidth of 200 MHz. The primary flux calibrators were 3C286 (C: 7.47 Jy) and 3C48 (X and U: 3.25 and 1.78 Jy respectively) and the phase calibrator was 1849+005 (J2000). The bootstrapped flux densities of the secondary calibrator were 0.83 Jy (C), 0.85 Jy (X) and 0.92 Jy (U). After editing and calibration the data were imaged using the AIPS task IMAGR with uniform weighting to maximize the resolution. The 5-GHz data were spatially filtered to only include data on baselines longer than 50 kλ to avoid contamination by the bright H II region G35.2S (see HL88). The half-power dimensions of the CLEAN beams were 0.57×0.37 arcsec^2 at a position angle of 49 degrees (C), 0.25×0.22 arcsec^2 at 33 degrees (X) and 0.14×0.13 arcsec^2 at 35 degrees (U). The VLA pointing centre is at RA(J2000)=18$^{\rm h}$58$^{\rm m}$12.93$^{\rm s}$, Dec(J2000)=+01°40′36.5″. Unfortunately high decorrelation in the U-band data meant that no images could be made.

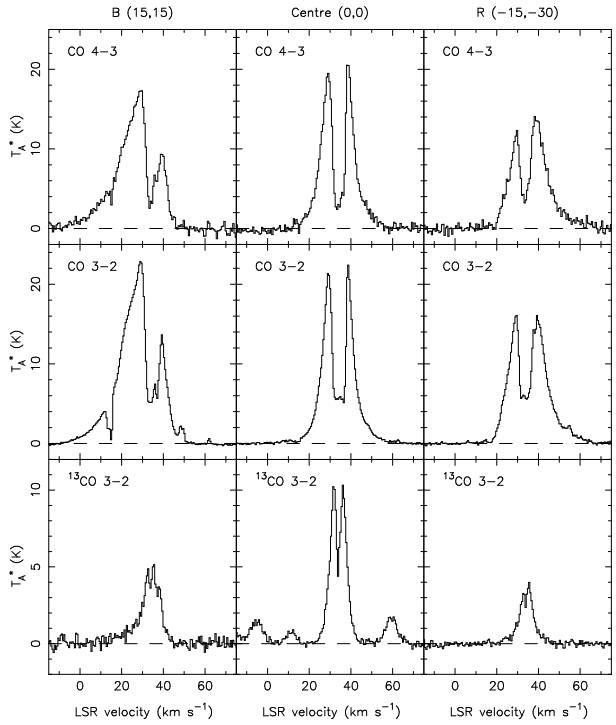

Figure 2. Example spectra from three positions in Fig. 1. Left panel is from peak position in the blue lobe (marked by an asterisk), centre panel is from the position of G35.2N and the right panel is from position marked by an asterisk in the red (south west) lobe. From top to bottom in each panel: ^{12}CO 4→3, 3→2 and ^{13}CO 3→2. The x-axis scale is velocity with respect to the LSR; the systemic velocity is +34 km s^{-1}. The dip in the ^{12}CO spectra at 15 km s^{-1} arises from a foreground cloud. The 'bumps' in the ^{13}CO spectrum at the centre position are lines of methanol observed in the upper sideband. Note the different vertical scale for the ^{13}CO spectra. The brightness temperatures in the figure may be converted to $T_{\rm R}^*$ assuming $\eta_{\rm fss}$=0.7.

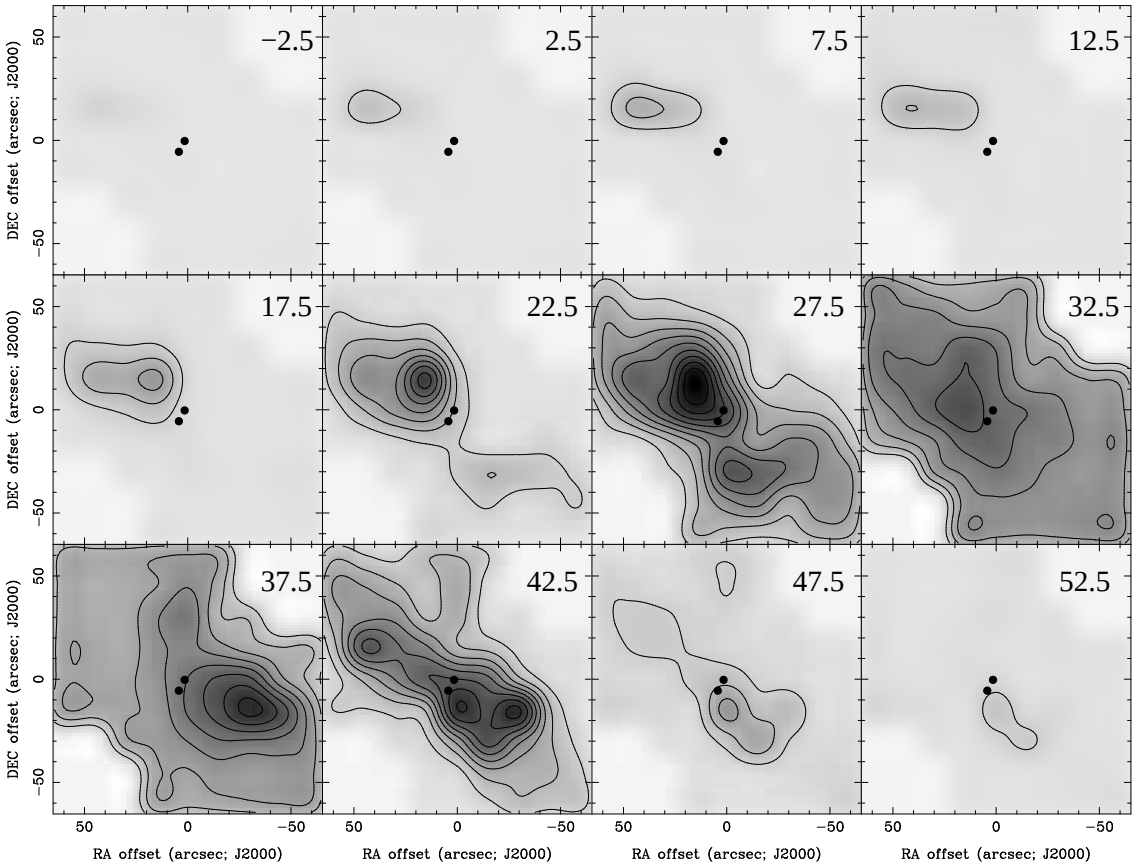

Figure 3. CO J=3→2 emission integrated over successive 5-km s^{-1}-wide velocity channels between 5 and 50 km s^{-1}. Lowest contour and interval are 10 and 10 K km s^{-1}. The centre velocity of each panel is given in the top right corner. The two filled circles mark the positions of G35.2N at (0,0) and G35MM2 at (2.8,–5.2) arcsec offset.

3 RESULTS

3.1 The CO outflow

Previous interpretation of the CO data has assumed the presence of a single driving source. The combination of our observations and other results show that there are multiple sources in this region, and it is likely that all contribute towards the observed CO distribution. The 3→2 CO blue- and red-shifted integrated intensity maps (Fig. 1) have a similar appearance to the 1→0 maps of Dent et al. (1985). Since the 3→2 line traces warmer and denser material than the 1→0 the detailed outflow structure is delineated more precisely. From these observations we find that the geometric centre of the outflow does not appear to coincide with the radio source G35.2N, and instead lies a few arcsec to the south-east. A new millimetre continuum source (see below) is a better candidate. Example CO 3→2 and 4→3 and ^{13}CO 3→2 spectra observed towards the blue and red lobes and central position are shown in Fig. 2.

The outflow clearly lies close to the plane of the sky, although the fact that the blueshifted emission in the north-east lobe is stronger than that in the south-west lobe (and vice versa for the red-shifted emission) shows that this lobe is inclined slightly towards us. The near-infrared reflection nebula (Walther et al. 1990) supports this geometry with its greater extent to the north of G35.2N. The apparent opening angle of the CO flow is ∼45 degrees. Assuming a biconical geometry the inclination probably lies between 0 and 23 degrees relative to the plane of the sky. Since there is substantial overlap between the red- and blue-shifted emission, an angle closer to 0 than 23 degrees seems most likely.

The blue lobe shows an S-like shape which is similar to what would be expected for an outflow driven by a precessing source (e.g. Cliffe et al. 1995). The red lobe does not have the same shape and in fact appears to be more collimated than the blue lobe with an unresolved jet-like appearance. A new feature not seen in the 1→0 data is the elongated red-shifted component extending to the north of centre. Due to confusion, it is difficult to tell whether it has a blue-shifted equivalent. This flow may be the molecular counterpart to the collimated radio jet (see below), and reinforces the interpretation that there are a number of separate outflows emanating from within the same molecular envelope, albeit with different orientations. Clearly higher-resolution observations are necessary to disentangle the outflow geometry near the driving sources.

Channel maps of the 3→2 emission are presented in Fig. 3. The lobes are not quite symmetric in their appearance with the north-east lobe extending beyond the edge of the mapped area. Furthermore the blue-shifted emission extends to a greater velocity relative to the LSR velocity than the red-shifted gas, 34 km s^{-1} (blue) compared with 15 km s^{-1} (red). The total velocity extent of the outflow to a noise level of 0.2 K is ∼50 km s^{-1}. The emission at the highest velocity is confined to a couple of 'hot spots' in each lobe of the flow, although they are not located symmetrically about the central source. The low-velocity material (best seen in the 32.5 km s^{-1} panel in Fig. 3) appears to delineate the edge of a cavity swept out by the outflow(s).

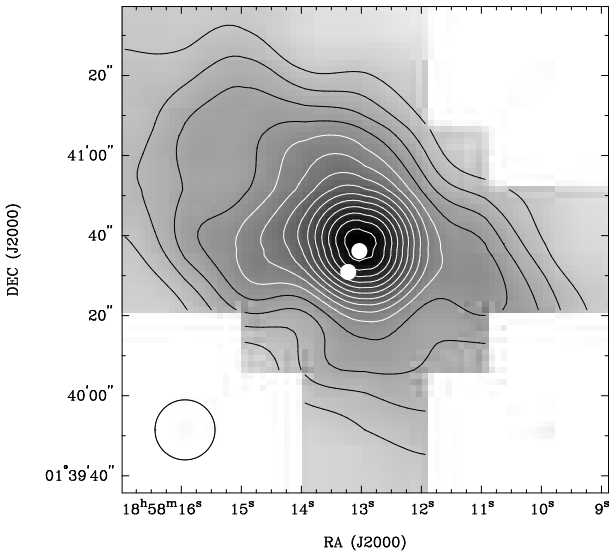

Figure 4. ^{13}CO J=3→2 emission integrated between 25 and 45 km s^{-1}. The contours start at 20 K km s^{-1} increasing in steps of 5 K km s^{-1}. The radio source G35.2N and millimetre source G35MM2 are each marked with a filled circle as in Fig. 1. The open circle in the bottom left hand corner represents the JCMT beam.

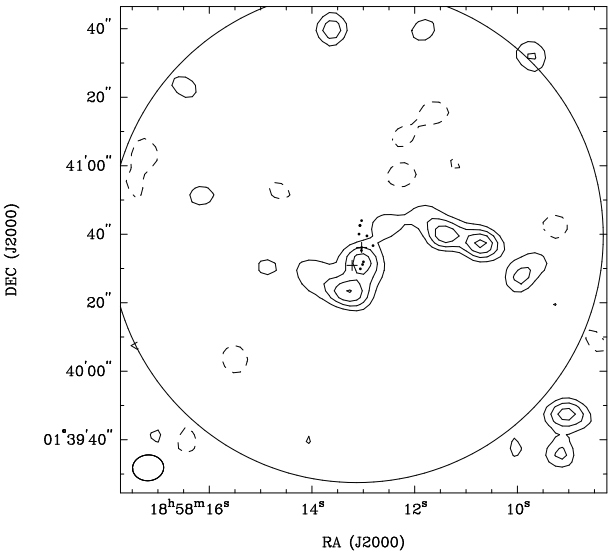

Figure 5. SiO J=2→1 emission integrated over the velocity range 31 to 37 km s^{-1}. The contours are –3σ, 3σ, then every 2σ to 15σ (σ = 0.8 K km s^{-1}). The crosses mark the radio source G35.2N and millimetre source G35MM2. Small filled circles mark the position of the radio sources from Table 1. The large circle is the primary beam FWHM of the BIMA antennas at 86 GHz and the ellipse represents the CLEAN beam.

A number of CO 4→3 spectra were recorded in order to facilitate calculation of the outflow parameters. Although severely self-absorbed (see Fig. 2), the 4→3 spectra indicate the presence of very warm gas. The shoulders of the self-absorbed 4→3 profiles imply temperatures of 40 K at the centre and in excess of 20 K within the outflow lobes (assuming the emission uniformly fills the beam). The 4→3 spectra also show the greatest velocity extent of all the CO spectra with emission extending to -45 km s^{-1} relative to the line centre at the eastern CO peak and +28 km s^{-1} in the south-west lobe.

3.2 CO isotopomers

The ^{13}CO 3→2 data (Fig. 4) are dominated by a central peak of emission coincident with the radio source G35.2N. The line is strongly self-absorbed at the centre, and many of the spectra show signs of self-absorption across the region mapped. The peak antenna temperature ($T_{\rm R}^{*}$) is 14 K, indicating a minimum excitation temperature of 21 K, although the line is heavily self-absorbed. Spectra are shown in Fig. 2. At low velocities the ^{13}CO also appears to trace the edge of the outflow cavity. From these data, the cavity has the appearance of a hollow cylinder, suggesting that the outflow does not continue expanding radially and that at least some of the collimation of the flow may be effected on large scales by the surrounding environment. At higher velocities, the central core of the flow is seen. The total velocity coverage to a noise level of 0.2 K is 18 km s^{-1}.

Emission from the C^{17}O 3→2 line is confined to a single symmetric spectrum at the central position with a brightness temperature of 0.67 K and linewidth 6.2 km s^{-1}. The noise level in these data is 0.1 K per 1 MHz channel (0.9 km s^{-1} at 337 GHz).

3.3 SiO 2→1 and 5→4 emission

The SiO 2→1 emission is shown in Fig. 5 integrated between 32 and 36 km s^{-1}. A number of interesting features are evident. Rather than show up in the outflow, the peak SiO emission appears located within the envelope around G35.2N, although it is offset by several arcsec to the south-east from the radio source, closer to the millimetre source G35MM2 (see below). There is no SiO emission which can be directly associated with the radio jet seen by HL88 (also see section 3.4 below). The SiO peak at (4,–13) arcsec offset from G35.2N does not appear to be associated with any known feature, although it does lie in a line which extends beyond the southern group of radio components. Further north towards the periphery of the BIMA primary beam half-power point, a knot of SiO emission lies along a line which can be traced back to the radio jet, some 50 arcsec to the south, and appears to be associated with the red-shifted spur seen in the CO data. This SiO maximum is also red-shifted, lying at ∼36 km s^{-1}.

In addition, the 2→1 SiO shows a linear feature composed of several knots of emission, extending parallel to the main CO outflow. This SiO feature may be tracing the shocked edge of a swept-out cavity, or it may be a separate well-collimated flow (see Fig. 5). Although not unprecedented, there is no evidence for the opposite lobe in this proposed outflow, neither in our CO nor in SiO. Higher-resolution CO observations may help distinguish it from the main CO flow.

Further observations are necessary to determine the reality of the components far from the phase centre, in particular the northern SiO knot and the linear feature. The majority of the SiO 2→1 emission seen in Fig. 5 is blue-shifted. The exception is the emission associated with the envelope which is red-shifted, peaking at 36 km s^{-1} with respect to the LSR.

A 5×3 grid with 20-arcsec spacing of 5→4 spectra orientated with the long axis along the outflow was observed with the JCMT. None of the spectra show significant emission (to a noise level of 85 mK in a 1.8 km s^{-1}-wide channel), although a map of the integrated intensity hints at a peak at the central position. Deeper integrations (to a noise level of 24 mK in a 1.8 km s^{-1}-wide channel) were made at the map centre and at the two CO peaks in the

north-east lobe. The 5→4 line was detected at the centre and the far CO peak at (45,15) arcsec offset (with an antenna temperature of ∼0.2 K). The 2→1 SiO data also show a peak at (45,15) arcsec offset from G35.2N, although it is only at the 3-σ level in Fig. 5. The 5→4 line was barely detected at the strongest blueshifted CO peak; thus it would seem that CO intensity is not necessarily a good indicator of where to search for SiO emission.

The 5→4 detections peak at different velocities: –0.5 km s^{-1} relative to the rest velocity at the centre and –7.5 km s^{-1} at (45,15) arcsec offset. The width of each line is ∼8 km s^{-1} (0,0) and ∼12 km s^{-1} (45,15). The 2→1 SiO emission does not appear to be as broad as that from the 5→4 line.

3.4 The radio jet

Fig. 6 shows the radio continuum images of G35.2N at 5 and 8.5 GHz. The data are broadly consistent with HL88 in that they show three main groups of components, one each to the north and south and one corresponding to the source itself. However, the higher resolution reveals structures not evident in the work of HL88. A total of 11 radio sources can be identified in the two images (see Table 1), although not all appear in both. The OH masers of Hutawarakorn & Cohen (1999) are distributed in a mostly linear geometry parallel to the large-scale envelope, and are shown by asterisks in Fig. 6. Source #7 in Fig. 6 lies close to several OH and H_2O masers and is most likely to be the driving source of the jet, which we refer to as G35.2N. The most striking result is that G35.2N itself is not detected at 5 GHz.

The 8.5-GHz image reveals that the weak component ∼3.5 arcsec to the west of the central source seen in the 15-GHz image of HL88 is genuine (source #6). A new point source (source #5) is detected 3.7 arcsec north-west of G35.2N, also not seen in the 5-GHz map. Fig. 6 also has the positions of H_2O masers taken from Forster & Caswell (1999). The majority of the OH masers are associated with the central source and are arranged along a line parallel with the major axis of the envelope (see below). Two of the water masers are associated with the southern group of radio components. They appear to lie upstream of the radio emission, suggesting perhaps that they arise in the dense molecular gas behind the shock. A study of their proper motions would confirm their association with the radio components. The clear association of water masers with shocks in outflows has only been seen before in two sources (Claussen et al. 1998; Wilner et al. 1999).

The size of the field in Fig. 6 is comparable with the 15-arcsec JCMT beam, but contains all of the radio sources. No radio emission is seen further away. The distribution of the radio components on the sky strongly suggests that they represent knots in a jet and that the jet is precessing. However, the implied half-angle of the cone defined by the precession is less than 10 degrees, which reinforces our earlier conclusion that the radio jet is probably not responsible for driving the large-scale CO outflow seen in Fig. 1.

3.5 The G35.2N envelope

The rotating clumpy envelope in which G35.2N is embedded was first delineated in ammonia by Little et al. (1985), and later by Brebner et al. (1987). Our 3.5 mm naturally-weighted continuum image (Fig. 7a) has the same centrally-peaked structure seen in the submillimetre dust continuum images of Dent et al. (1989) and Vallée & Bastien (2000). The deconvolved dimensions from a two-dimensional gaussian fit are 22×13 arcsec^2 (0.21×0.13 pc^2 for a source at 2 kpc) at a position angle of 42 degrees west of north, consistent with the above dust observations. The similar appearance of the 3.5-mm continuum and the submillimetre dust emission suggests that our BIMA observations are tracing cool, extended dust emission. The 3.5-mm continuum image extends along the direction of the northern jet components, and even further north-west out to encompass the north-west ammonia peak in the maps of Brebner et al. (1987) and Little et al. (1985).

Observations of G35.2N made with OVRO (J.M. Carpenter, private communication) reveal the presence of a second dust emission peak, coincident with the main NH_3 (3,3) peak of Brebner et al. (1987) and close to the SiO 2→1 peak in Fig. 5. Carpenter has labelled this source G35MM2. Unfortunately our data do not have the spatial resolution to confirm this but we do find that our $H^{13}CN$ and $H^{13}CO^+$ line emission does peak at the position of G35MM2 (see below). However, G35MM2 has no radio counterpart in Fig. 6 to a 4σ level of 0.1 mJy per beam at 8.5 GHz.

The $H^{13}CO^+$ and $H^{13}CN$ 1→0 integrated intensity maps are shown in Fig. 7. The $H^{13}CO^+$ integrated emission peaks on the (3,3) ammonia peak of Brebner et al. (1987), coincident with G35MM2 while the $H^{13}CN$ peaks on G35.2N. The emission from both molecules exhibits the same north-west to south-east velocity gradient observed in ammonia of Little et al. (1985). (It should be noted the labelling of the channel maps of Little et al. are reversed.) The velocity shift from north-west to south-east is ∼4 km s^{-1}.

Fig. 8 shows channel maps demonstrating the velocity gradient across the envelope. The envelope appears reasonably continuous, although there is evidence of structure on scales smaller than the ∼10-arcsec beam. The envelope is not resolved along the minor axis. At the ambient velocity, the $H^{13}CO^+$ peaks on G35MM2, although it extends north-west to include the location of G35.2N itself. At 32 km s^{-1} the envelope extends 30 arcsec to the north-west and shows a change in the position angle. This emission is elongated and coincides with the weaker (3,3) ammonia peak of Brebner et al. (1987). This peak is close to the SiO 'jet' described above and may represent the location of the driving source.

The brightness temperature of the $H^{13}CO^+$ emission is remarkably uniform across the envelope at 2.5 to 3 K away from the central position. The peak line brightness is 3.9 K towards G35MM2 where the linewidth is 4.0 km s^{-1}; at the position of G35.2N the line is slightly weaker at 3.5 K but broader at 5.2 km s^{-1}. A weak blue wing is seen in both of these spectra which is absent further from the centre of the core.

The $H^{13}CN$ emission has qualitatively the same appearance as the $H^{13}CO^+$ (Fig. 9), although interpretation of the velocity structure is complicated by the blending of the F=2→1 and F=1→1 hyperfine components which are separated by 4.86 km s^{-1}. The $H^{13}CN$ peaks more towards G35.2N, and also has a peak brightness temperature of ∼3 K. Linewidths derived from Gaussian fits to the $H^{13}CN$ hyperfines are poorly constrained due to blending of the hyperfine components but the linewidth peaks at the position of G35.2N at ∼5.5–6.0 km s^{-1}, decreasing to 4.5–5.0 km s^{-1}at the position of G35MM2. Further away from the centre, only the stronger two hyperfines are detected with even lower linewidths (around 2–2.5 km s^{-1}).

Since the excitation of the 1→0 lines of $H^{13}CN$ and $H^{13}CO^+$ is similar, it seems surprising that one is broader than the other. Perhaps the greater linewidth derived from the $H^{13}CN$ data implies that these lines may be tracing more turbulent gas closer to the embedded sources, or a component which is swept up in the outflows from each source. Alternatively, since the $H^{13}CN$ beam is slightly larger than that for $H^{13}CO^+$ it could be tracing more of the system-

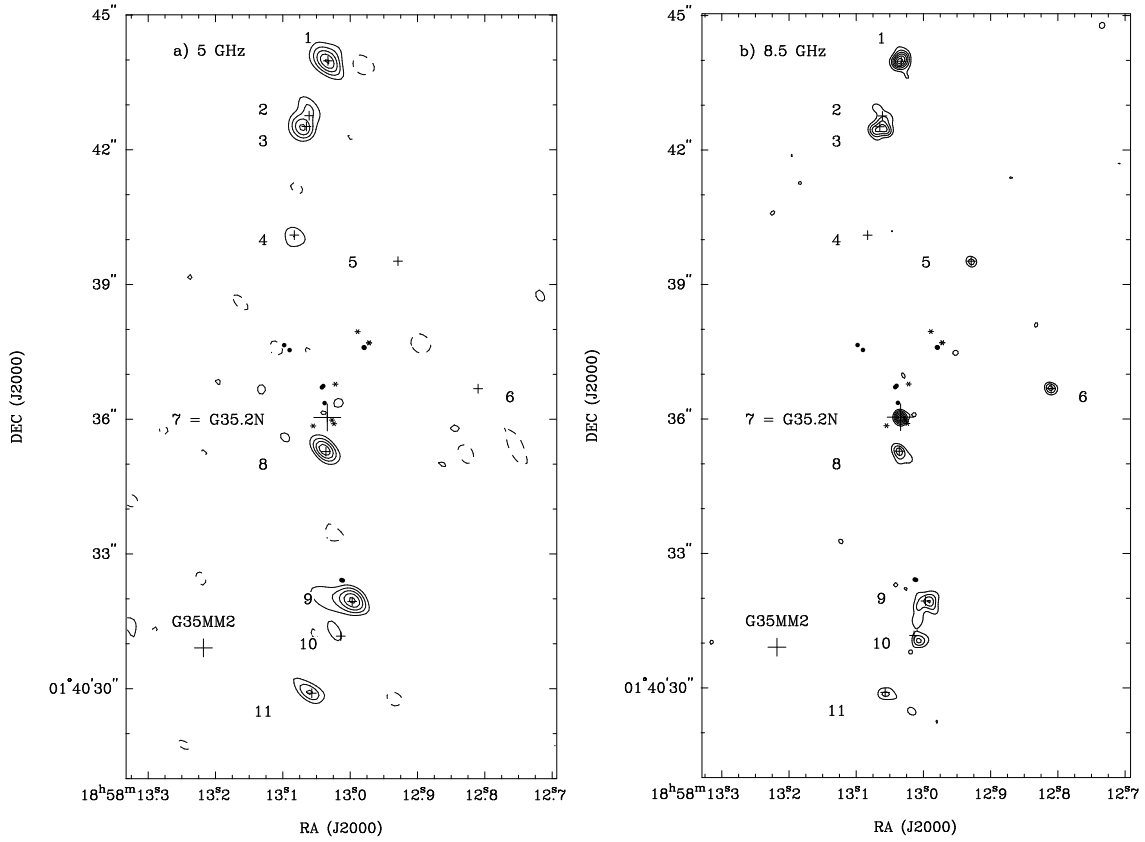

Figure 6. a) 5-GHz radio continuum emission from G35.2N. The contours are at –5,3,5,7,9,11,13,15×60μJy per beam. The beam is 0.57×0.37 arcsec^2 at a position angle of 49°. b) 8.5-GHz radio continuum emission from G35.2N. The contours are at –5,3,5,7,9,11,13,15×33μJy per beam. The beam is 0.25×0.22 arcsec^2 at a position angle of 33°. In both images the positions of OH and H_2O masers from Hutawarakorn & Cohen (1999) and Forster & Caswell (1999) are marked by asterisks and filled circles respectively. The radio sources listed in Table 1 are marked by small crosses. The millimetre source, G35MM2, is also marked with a cross.

Table 1. Radio source parameters. The position offsets are in arcsec from G35.2N, located at RA(J2000)=18^{h}58^{m}13.02^s, Dec(J2000)=01°40′36.20″ Spectral indices are derived from the fluxes given in columns 7 and 8, measured from the tapered images (see text). The uncertainty in the peak/total fluxes is 0.06 mJy per beam/0.15 mJy at 5 GHz and 25 μJy per beam/50 μJy at 8.5 GHz. In the tapered maps the uncertainties in the total fluxes listed are typically 0.1–0.2 mJy.

Source	Offset	5-GHz flux		8.5-GHz flux		Tapered flux		Spectral
	(arcsec)	Peak	Total	Peak	Total	5-GHz	8.5-GHz	index
1	(0.0,7.8)	0.66	1.0	0.45	1.0	1.0	0.9	–0.2±0.4
2	(0.4,6.5)	0.40	0.7	0.22	0.5	–	–	–
3	(0.5,6.4)	0.56	0.8	0.34	1.1	0.9	1.4	0.8±0.4
4	(0.7,3.9)	0.30	0.4	<0.05	<0.1	0.2	<0.1	–1.3±0.4
5	(–1.5,3.4)	<0.13	<0.2	0.20	0.2	<0.1	0.2	>1.3
6	(–3.3,0.5)	<0.13	<0.1	0.28	0.3	–	–	–
7	(0,0)	<0.20	<0.2	0.48	0.5	<0.2	0.4	>1.3±1.4
8	(0.1,–0.9)	0.66	0.6	0.25	0.6	0.3	0.4	0.5±1.1
9	(–0.4,–4.2)	0.70	1.0	0.25	1.2	1.3	1.0	–0.5±0.3
10	(–0.3,–5.0)	0.26	0.3	0.23	0.5	0.3	0.4	0.5±1.1
11	(0.4,–6.2)	0.44	0.5	0.18	0.4	0.6	0.5	–0.3±0.7

atic velocity gradient along the core. This seems unlikely since the extra contribution to the $H^{13}CN$ linewidth from the velocity gradient (13 km s^{-1} pc^{-1}: see below) in the additional 1.3 arcsec may be estimated to be only ∼0.16 km s^{-1}. Finally, the blending of two of the hyperfine components may be biasing the Gaussian fits towards larger values for the linewidth.

The observed ratio of the $H^{13}CN$ hyperfine components is consistent with optically thin emission from molecules in local thermodynamic equilibrium (LTE) at all positions. An upper limit to the total optical depth is ∼0.1 (equal to the sum of the optical depths of each hyperfine component).

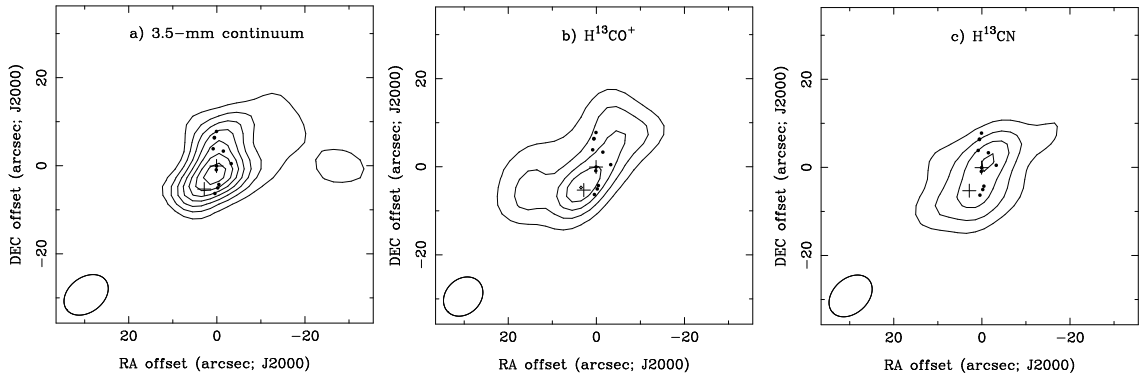

Figure 7. a) BIMA 3.5-mm continuum emission (made with natural weighting). The peak flux is 82 mJy beam^{-1} and the beam is 11.1×7.9 arcsec^2 at –53°. b) H^{13}CO$^+$ 1→0 and c) H^{13}CN 1→0 average intensity over the velocity range 32 to 36 km s^{-1} (covering the main F=2→1 hyperfine of H^{13}CN). In each panel the contours are spaced by -3, 3, 5, 7, 9, 11, 13, 15 times the noise level (8 mJy per beam, 0.3 K and 0.3 K respectively). The radio sources are marked by filled circles with G35.2N and G35MM2 marked by crosses. Each image is centred on G35.2N.

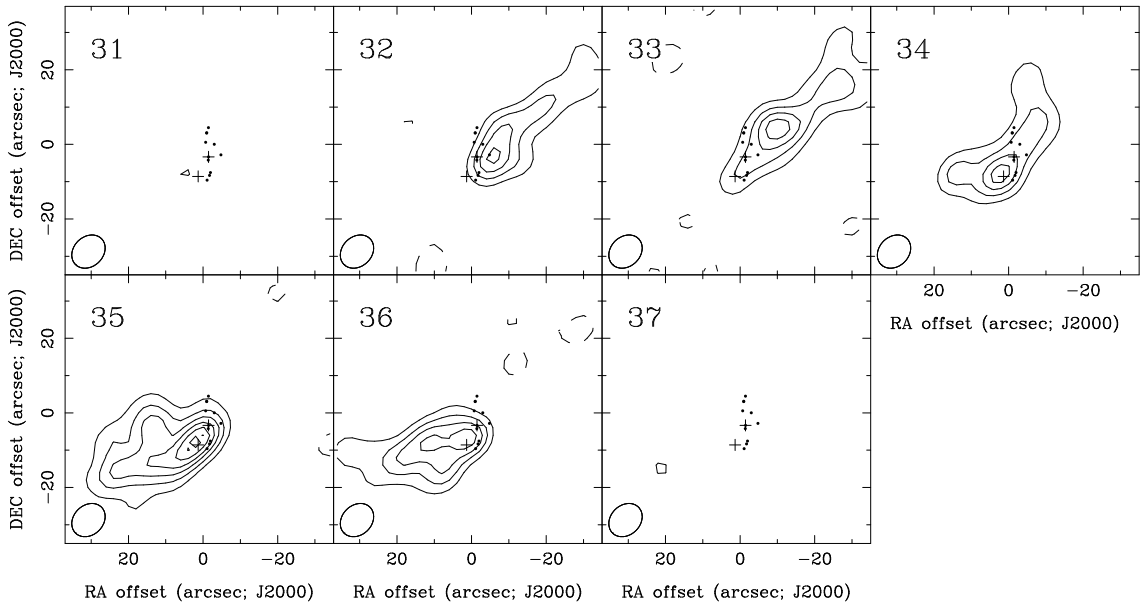

Figure 8. H^{13}CO$^+$ 1→0 emission integrated over five successive 1- km s^{-1}-wide velocity intervals from 31 to 37 km s^{-1}. In each panel the contours are spaced by -3, 3, 5, 7, 9, 11, 13, 15 times the noise level (∼0.3 K). The radio sources are marked by filled circles with G35.2N and G35MM2 marked by crosses. The image is centred on G35.2N. The CLEAN beam is 9.8×7.9 arcsec^2 at –46°. The velocity of each panel is printed in the top left.

4 ANALYSIS

4.1 Outflow parameters

While the data presented in Section 3 demonstrate that there are probably several outflows, it is not obvious how they should be separated and so the following analysis examines the whole of the high-velocity emission.

The outflow parameters have been calculated using standard analysis techniques (e.g. Bally & Lada 1983), initially assuming optically thin emission and that the level populations are characterized by a single excitation temperature at all velocities. Minimum values for the mass, momentum and kinetic energy can be derived assuming an excitation temperature equal to the energy of the upper level (Macdonald et al. 1996), which is ∼33 K for the J=3 level of CO. A CO abundance of 10^{-4} relative to H_2 was assumed. The choice of the velocity range to exclude from the calculation is determined in part by the amount of the line affected by the severe self-absorption. We have chosen to ignore emission less than 4 km s^{-1} away from the line centre (in accord with Little et al. 1985).

If the optical depth, τ, is non-negligible, then the mass and outflow energetics will be underestimated by a factor of $\tau/(1-e^{-\tau})$. We have estimated the optical depth by comparing ^{12}CO and ^{13}CO 3→2 spectra recorded at the same positions across the outflow (see e.g. Lada 1985). We have assumed the [^{12}CO]/[^{13}CO] ratio is 75. This analysis shows that over the velocity range considered, the beam-averaged optical depth generally falls monotonically from a value of ∼3–5 (at velocities 4 to 6 km s^{-1} from the line centre) to less than ∼1 at velocities greater than about 10 km s^{-1} from the line centre. The signal-to-noise ratio is not high enough to extend beyond 10 km s^{-1}. The mean value between 4 and 10 km s^{-1} from the line centre is ∼2–3. The fraction of material lying at the lower velocities corresponds to about half the calculated mass, which means that by assuming low optical depth (and that the emission uniformly fills the beam), we are underestimating the

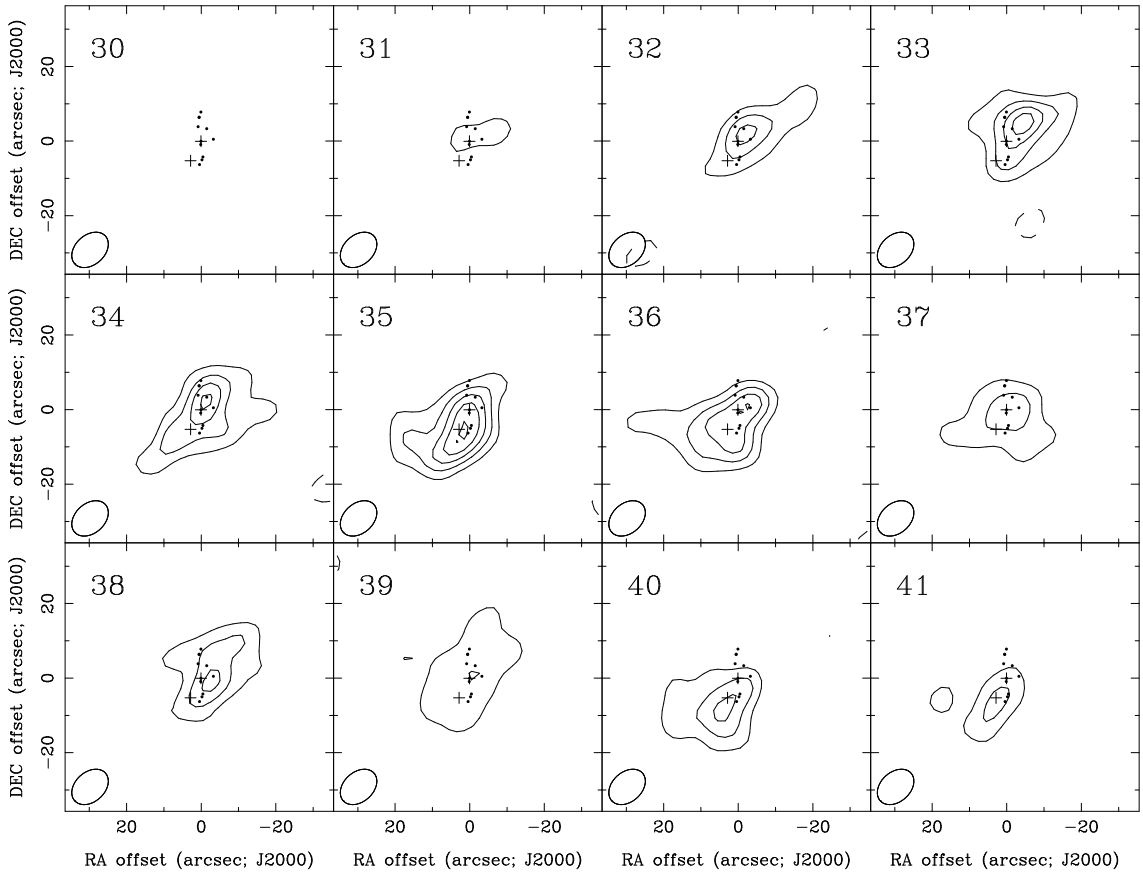

Figure 9. $H^{13}CN$ 1→0 emission integrated over successive 1- km s^{-1}-wide velocity intervals from 30 to 41 km s^{-1}. In each panel the contours are spaced by -3, 3, 5, 7, 9, 11, 13, 15 times the noise level (∼0.3 K).The radio sources are marked by filled circles with G35.2N and G35MM2 marked by crosses. The image is centred on G35.2N. The CLEAN beam is 11.1×7.9 arcsec^2 at –48°. The velocity of each panel is printed in the top left.

Table 2. Outflow parameters. No correction for optical depth or inclination has been applied to these values. No attempt has been made to distinguish individual flows.

Parameter	Red lobe	Blue lobe
Mass ($M_\odot$)	3.7	7.7
Momentum ($M_\odot$ km s^{-1})	31.3	81.7
Energy (erg)	3.2(45)	12.4(45)
Size (pc)	0.37	0.37
Mean velocity (km s^{-1})	8.3	10.6
Timescale (yr)	4.3(4)	3.4(4)
Luminosity ($L_\odot$)	0.59	2.9
Force ($M_\odot$ km s^{-1} yr^{-1})	7.3(–4)	2.4(–3)

total outflow mass by about a factor of two. The momentum and kinetic energy of the flow are less susceptible to the effects of finite optical depth since they are weighted by velocity, and the highest velocity material has the lowest beam-averaged optical depth.

From the results above we can fit the optical depth with a function that falls off with velocity as a power law of the form $\tau(v) \simeq 57/v^{1.7}$. This reproduces the three values quoted above to within 10 per cent. We can use this to make a correction for optical depth with velocity for the outflow since. Assuming such a power law, the optical depth does not get below 0.1 until a velocity 45 km s^{-1} from the line centre is reached, a velocity which is equal to or higher than the maximum velocity in each lobe.

Table 2 lists the relevant outflow parameters with the above optical depth correction applied. The size is the intensity-weighted mean distance from the central source. The mean velocity is calculated from the ratio of the momentum to the mass. The luminosity is the product of the energy and the dynamical timescale, while the force is the momentum divided by the dynamical timescale. In addition, no attempt has been made to separate the two outflows, although the jet-flow is likely to contribute only a small amount to the total.

Comparison of our results with the 1→0 results of Little et al. (1985) reveals a large discrepancy. For example, we calculate the outflow mass as ∼11 $M_\odot$ here compared with 30 $M_\odot$ (correcting the value of Little et al. for the different CO abundance). Excitation effects probably account for the large discrepancy between the two values. The 3→2 line is excited in denser gas, and thus its emission will arise from a smaller area. It is unlikely that assuming 30 K as the excitation temperature contributes significantly to the difference in 1→0 and 3→2 CO mass estimates as the fraction of molecules in the J=3 level decreases by only 50 per cent if we choose a temperature as low as 15 K, or as high as 100 K. The observed ratio of the 3→2 and 4→3 lines unfortunately places little constraint on the excitation temperature. The ratio of the mean spectra has a roughly constant value of 1.1±0.2 at all velocities where the sensitivity is high enough, consistent with our assumption of 33 K (assuming that the gas uniformly fills both beams). There is also a weak trend for the higher-velocity material to have a higher excitation temperature.

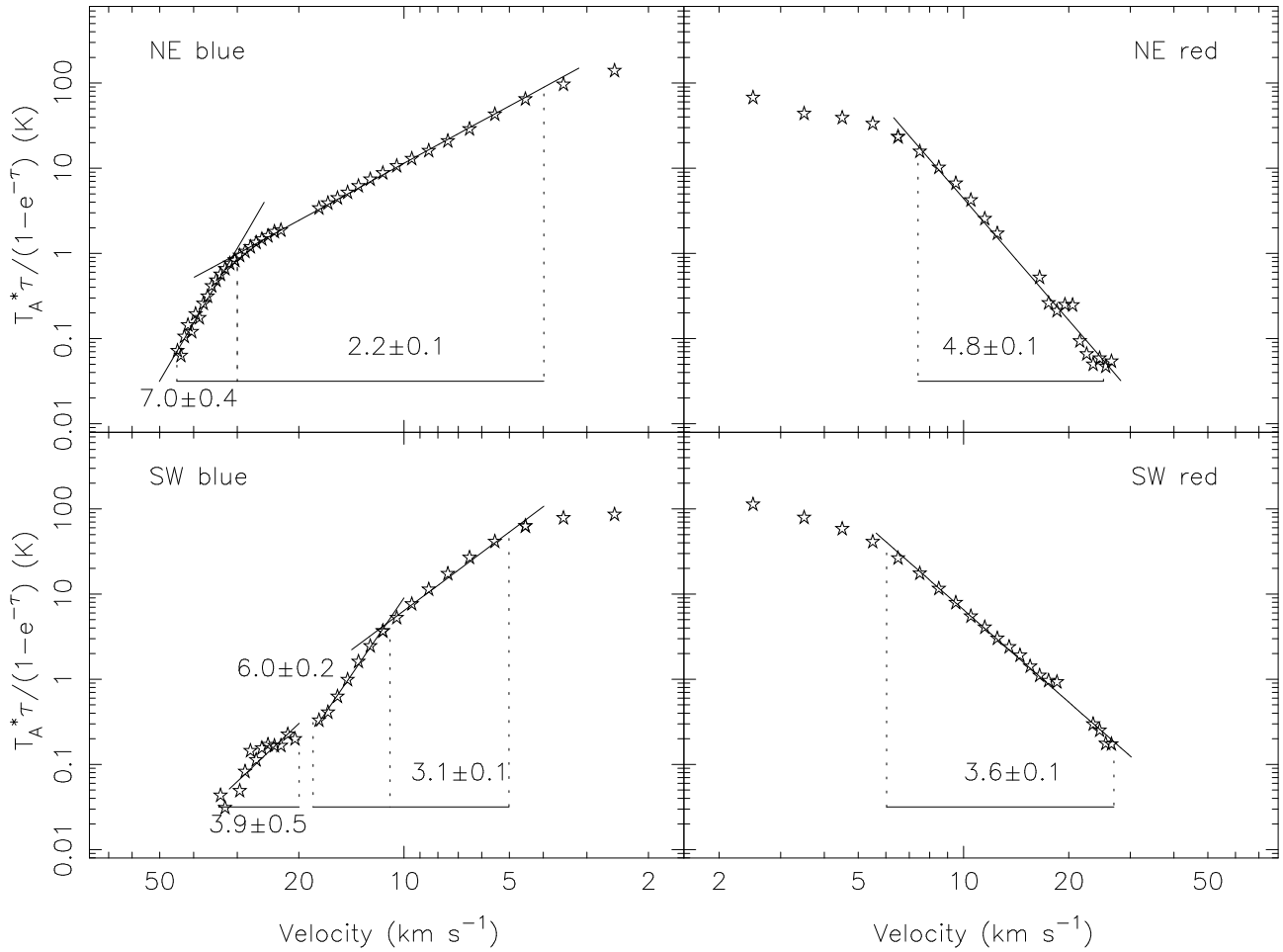

Figure 10. Mass-velocity plots for the red- and blueshifted gas in both the north-east and south-west lobes. One or more power-laws have been fitted to the data, and the index is shown in each panel. a) Velocity ranging from 5–45 km s^{-1} from the rest velocity (34 km s^{-1}) b) 6–25 km s^{-1}, c) 6–34 km s^{-1}, and d) 7–27 km s^{-1}. The gaps at ∼15–20 km s^{-1} where data have been removed from the fit probably represent an unrelated molecular cloud along the line of sight.

Table 3. Listing of γ as derived from fits to each lobe, both for uncorrected ('raw') data and optical depth-corrected data ('corr'). The fits are plotted on Fig. 10 over the ranges given in this table.

Lobe	Velocity Range (km s^{-1})	$\gamma_{\rm raw}$	Velocity Range (km s^{-1})	$\gamma_{\rm corr}$
NE blue	5–10	1.0±0.1	5–30	2.2±0.1
	10–30	2.0±0.1		
	30–44	6.6±0.4	30–44	7.0±0.4
NE red	9–25	4.9±0.4	6–25	4.8±0.4
SW blue	6–11	2.4±0.1	6–11	3.1±0.1
	11–18	5.5±0.2	11–18	6.0±0.2
	20–34	3.2±0.5	20–34	3.9±0.5
SW red	7–27	2.8±0.1	7–27	3.6±0.1

We have also calculated (and plotted in Fig. 10) the mass as a function of velocity for each lobe to investigate its usefulness in constraining models of outflows. We have again assumed that the emission is characterized by a constant excitation temperature and uniformly fills the beam at all velocities, so that the outflow mass as a function of velocity is directly proportional to the observed brightness temperature (summed over all spectra in the lobe) at that velocity corrected for optical depth. We have fitted power laws of the form $v^{-\gamma}$ to the data. We find that not only are these power laws different from the $v^{-1.8}$ found by Masson & Chernin (1992), but that a single power law does not always reproduce the variation of mass over the whole velocity range. In both the red- and blue-shifted gas there are velocity ranges which have indices much greater than 2, most notably for the highest-velocity blue-shifted gas which has a value for γ as high as 7.0 in the north-east lobe (Fig. 10). However, it is remarkable that with the optical depth correction applied, the north-east blue lobe does have a value of γ close to 2 which fits the data out to 30 km s^{-1} from the line centre. The north-east blue lobe also shows a turnover in γ at the highest velocities, a feature seen in a number of other outflows (Fich & Lada 1997; others?). The other lobes do not show such a turnover, but they also do not extend as far in velocity.

4.2 SiO excitation

With the two transitions of SiO we have been able to apply a radiative transfer code (which employs the large velocity gradient or LVG approximation: Goldreich & Kwan 1974) to try and constrain some of the parameters of the shocked gas in the outflow. We used it in two ways: in the first we made no correction for the difference

in beamsize, and in the second we constructed a 2→1 image with a 22-arcsec restoring beam from which we then obtained spectra.

We attempted to model the lines from the position of MM2, but we were only able to place some limits on the gas parameters. The modelling confirmed some general intuitive conclusions regarding the excitation of SiO in the shocked gas; either a low density/high abundance or high density/low abundance solution, with the temperature remaining relatively low (30–50 K). The high-density ($\sim$few$\times10^6$ cm^{-3}) solutions were found at the lower temperatures.

The main difficulty with deriving the gas parameters from the SiO data is that the emitting area is very much smaller than the 22-arcsec beam (and even the 10-arcsec BIMA beam). The models of Schilke et al. (1997) predict an SiO-emitting region of order 10^{16} cm in length, which corresponds to 0.33 arcsec at the distance to G35.2N (2 kpc). This means that the beam-averaged parameters generally are not good estimates of the true parameters, and probably underestimate the true density in the SiO emitting regions by an order of magnitude or more.

Are we missing any extended SiO emission? Codella, Bachiller & Reipurth (1999) show that towards some outflow sources the lower J SiO emission (2→1 and 3→2) has a diffuse extended component compared with the 5→4 emission. In addition, interferometric observations of HH7–11 show that only 10 per cent of the SiO flux is recovered (Bachiller et al. 1998). If the SiO 2→1 emission associated with the G35.2N region is extended then our BIMA observations may be missing a significant fraction, leading to erroneous conclusions regarding its distribution and excitation. It is difficult to know whether this is the case without single-dish observations of the 2→1 SiO line. The effect of missing flux on our LVG modelling will be to lower the 5→4/2→1 ratio, most likely leading to solutions which favour lower density and/or temperature.

4.3 The properties of the envelope

A two-dimensional gaussian fit to the 3.5-mm continuum emission yields source dimensions of 22×13 arcsec^2 at a position angle of –42 degrees. The peak flux in the model is 71 mJy beam^{-1} and the total flux is 241 mJy. If the radio sources have the spectral indices listed in Table 1 then they could contribute up to 20 mJy at 86 GHz. This is roughly 10 per cent of the total, but since most of the radio emission is confined to a single BIMA beam, it is possible that the emission from the wind contributes a significant fraction (30 per cent) to the peak flux at the position of G35.2N. Observations at intermediate frequencies and higher resolution millimetre observations are necessary to determine the exact contributions of the free-free emission.

Assuming a dust temperature of 30 K (Dent et al. 1989), we derive masses for the whole envelope of between 600 and 1400 $M_\odot$ from the 3.5-mm continuum data, depending on the value and frequency-dependence of the absorption coefficient (Hildebrand 1983; Mezger et al. 1987).

The $H^{13}CO^+$ emission shows a velocity gradient along the long axis of the envelope of 13 km s^{-1} pc^{-1}, which translates to a rotation period of 75000 years. A position-velocity cut along the long axis (shown in Fig. 11) shows that the velocity gradient is not uniformly smooth, but appears to show evidence for three velocity components within the envelope, one at 32.5 km s^{-1} (to the north-west), one at the systemic velocty of 34 km s^{-1} and one at 35 km s^{-1} (to the south-east). Thus the envelope is not continuous but fragmented into a number of cores each harbouring one or more YSOs. Alternatively the $H^{13}CO^+$ may be tracing components

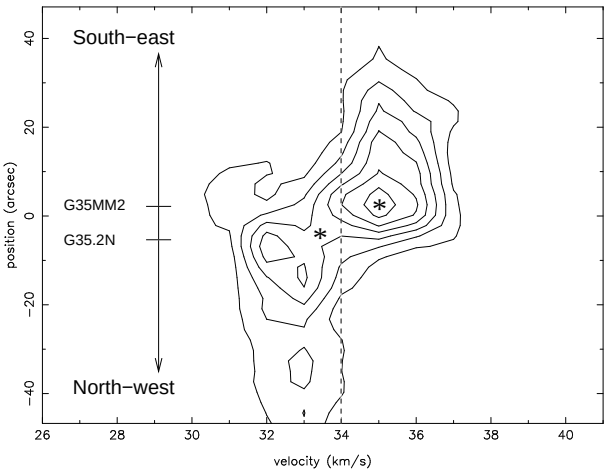

Figure 11. Position-velocity diagram for the $H^{13}CO^+$ emission. The y-axis represents offsets in arcsec along the cut which has a position angle of 55 degrees west of north. The positions along the cut of G35.2N and G35MM2 are labelled and marked by asterisks.

of the outflow, blue-shifted in the north-west and red-shifted in the south-east. However, this may be true only for the extreme red- and blue-shifted $H^{13}CO^+$ emission since the same velocity gradient is observed in the ammonia data of Little et al. (1985).

Virial masses may be derived from the linewidths given above. For a uniform sphere, the virial mass is given by $M_{\rm vir} = 209\Delta v^2 r\,{\rm M}_\odot$, where Δv is the linewidth in km s^{-1} and r is the radius in pc (taken to be the appropriate beam radius). At the position of G35.2N, the virial mass is estimated to be $\sim$350 $M_\odot$, decreasing to $\sim$210 $M_\odot$ at the position of G35MM2. These masses are larger than those derived from the ammonia observations of Little et al. (1985) which suggests that the $H^{13}CN$ may be tracing regions with enhanced velocity dispersion, probably the outflow.

From the brightness of the $H^{13}CN$ lines and assuming a total optical depth of 0.1 (see above) we derive excitation temperatures of 50 and 45 K at the positions of G35.2N and G35MM2 respectively, assuming the emission uniformly fills the beam. These are higher than previous estimates (typically 30 K; Little et al. 1987), consistent with tracing warm material close to the embedded sources. Assuming optically thin LTE emission, a column density of 1.6×10^{14} cm^{-2} is derived for $H^{13}CN$ towards G35.2N. The virial mass above translates to a molecular hydrogen column density of 3.6×10^{24} cm^{-2}, which implies an abundance of 4.4×10^{-11} for $H^{13}CN$. The $H^{13}CN$ abundance is not well determined but using an abundance for the main isotopomer of 2×10^{-8} (Irvine, Goldsmith & Hjalmarson 1987) and assuming a $^{12}C/^{13}C$ ratio of 75 a value of 2.7×10^{-10} may be derived. An alternative estimate for the $H^{13}CN$ abundance may be derived by comparing the dust mass above with the estimate for the envelope from the $H^{13}CN$ lines. This method give a value of $\sim1.1\times10^{-10}$ with a 50 per cent spread in values. These calculated values are factors of 2 to 5 smaller than that derived from the value given by Irvine et al. (1987). This may indicate that HCN is freezing out onto dust grains near the centre of the core, but given the large uncertainties in both the H_2 column density and the 'standard' value for the $H^{13}CN$ abundance we regard this conclusion as tentative at best.

Since the $H^{13}CO^+$ is not tracing gas as close to the embedded sources as the $H^{13}CN$ (see section 3.5), the excitation temperature

for the $H^{13}CO^+$ will be lower. We will assume a value of 30 K as appears to be appropriate for the less dense gas. A $H^{13}CO^+$ column density of 4.0×10^{13} cm^{-2} is derived at the centre of the envelope.

4.4 The nature of the radio components

The majority of the radio components detected (sources #1–4 and 8–11) lie along a line which suggest they are part of a collimated jet driven by G35.2N. There are two which probably are not and which may be individual YSOs or extragalactic in nature. Since these are seen at 8.5 GHz but not at 5 GHz they have a positive spectral index and therefore are most likely to be YSOs. Source #6 lies between two of the mid-infrared sources detected by Fuller et al. (2001), and was suggested by these authors to be responsible for a separate outflow. Within the small field imaged ($<$ 20 arcsec diameter) we may expect to detect $<$1 extragalactic source at 8.5 GHz (Anglada et al. 1999).

We have calculated spectral indices (assuming total flux density $\propto \nu^{\alpha}$) for all the components which show up at both 5 and 8.5 GHz and placed limits on those which are visible at only a single frequency. To avoid problems with differing beamsizes, both maps were tapered to give beams with similar half-power dimensions of 0.65×0.56 arcsec. The required taper was 300 kλ at 5 GHz, and 220 kλ at 8.5 GHz. The noise in each image was similar at 75–80 μJy per beam. The spectral indices are listed in Table 1. Those sources without spectral indices were only present in the full-resolution images.

The uncertainties in the calculated spectral indices are significant and in most cases it is difficult to unambiguously determine the emission mechanism responsible for each component. Sources #5, #6 and #7 have clearly positive spectral indices, and therefore probably mark the location of embedded luminous YSOs. In particular #7 is the source of the jet due to its location with respect to the OH and water masers in the region (Fig 6). For the remaining components it seems likely that the spectral indices are consistent with optically thin thermal free-free or weak gyrosynchrotron emission.

Models of radio emission from shocks can account for both negative and positive spectral indices, but not with a single model (Henriksen et al. 1991; Ghavamian & Hartigan 1998). In G35.2N, therefore, the mechanism must be different in each case and it suggests that the shocks in outflows from massive YSOs contain weakly relativistic electrons. In this respect, G35.2N differs from the other well-known radio jet sources such as HH80–81 (Martí et al. 1993), W3-H_2O (Wilner et al. 1999) and Serpens (Rodríguez et al. 1989). All these sources appear to have symmetric jets with negative (and equal) spectral indices for components in either direction from the central source.

4.4.1 Extended radio emission: an ionized cavity

It is instructive to compare the 5-GHz flux in our A-configuration map with the fluxes derived from the lower-resolution observations of Dent, Little & White (1984) and HL88. From such a comparison we conclude that there is evidence for an evacuated cavity which contains ionized gas. This cavity is associated with the jet source, G35.2N. Furthermore it may be that weak emission has been detected along the path of the beam of the jet itself.

Dent et al. (1984) derive a total of $\sim$14 mJy for their double-peaked structure. An extended ('diffuse') component is observed in their data, contributing about 40 per cent of the total flux density. HL88 measure a total flux density of $\sim$8 mJy, about 60 per cent of that of Dent et al. (1984). These authors deduce that a gaussian source with FWHM dimensions 10×2 arcsec^2 can account for the difference between the two measurements. Such a source may represent extended emission from ionized gas within a cavity swept out by the jet and/or a stellar wind.

The total 5-GHz flux density in our data is $\sim$5.4 mJy, or 68 per cent of the HL88 flux, suggesting that our A-configuration observations are further resolving out the emission. The flux missing from our 5-GHz image is probably from the extended feature seen in the HL88 image which links the northern group of components with the central region. This may be ionized material within the jet itself or at the shocked boundaries of the jet and ambient cloud.

5 DISCUSSION

5.1 Precessing outflows in G35.2–0.7N?

It has long been suspected that the driving source for the CO flow is precessing (HL88, Little et al. 1998). The 3$\rightarrow$2 CO data appear to support this interpretation. The blue lobe in particular (Fig. 1a) has an 'S'-shape similar to that expected for a precessing flow (e.g. Cliffe, Frank & Jones 1996). The problem with this interpretation has always been the large offset in position angle between the radio jet (roughly north-south) and the CO flow (58 degrees east of north).

The data presented in this paper help to resolve this issue, showing that there are perhaps as many as four outflows, all of which contribute to the overall CO appearance: 1) the radio jet and CO flow from G35.2N; 2) the CO flow from G35MM2; 3) the SiO flow; and possibly 4) the flow driven by radio source #6 (only observed indirectly through the infrared observations of Fuller et al. 2001).

The CO flow associated with the radio jet is primarily identified from the finger of redshifted CO emission seen in Fig. 1, although it is also evident at velocities close to the systemic velocity (see the 32.5 km s^{-1}-panel in Fig. 3), which suggests that it lies close to the plane of the sky. However, the fact that the infrared reflection nebula is brighter in the north suggests that it is tilted towards us, so that CO emission from the jet outflow should be blueshifted. In general the assumption that a bright reflection nebula indicates an region inclined towards us is based on the cloud in which the nebula is embedded being uniform. If, say, the G35.2N cloud is denser to the south and west then the southern lobe of a reflection nebula will be more heavily extinguished compared with the northern lobe, especially if the outflow is close to the plane of the sky. Such a geometry would yield a brighter northern reflection nebula despite being tilted away from us provided the inclination to the plane of the sky was not significant as appears to be the case here.

The superposition of multiple flows with slightly different position angles can account for the impression of a single precessing flow. Therefore a precession interpretation seems unnecessary. However, it is likely that the driving sources of at least two of the flows are themselves precessing. The radio data *do* appear to show clear evidence for a precessing jet, with the individual knots of radio emission showing offsets of upto an arcsecond from a projected straight line through the central source and curving away at each end of the jet (Fig. 6). The peaks in the CO flow (Fig. 1) do not lie along a straight line which suggests that the flow from G35MM2 is also precessing.

5.2 The mass-velocity relation

The question of whether the mass-velocity index (γ, where $m_v \propto v^{-\gamma}$) places a useful constraint on outflow models remains unanswered. Masson & Chernin (1992) derived a value of 1.8 for several flows, while a number of recent observational studies have shown that mass at high-velocity decreases more rapidly than as v^{-2} (Davis et al. 1998, Gibb & Davis 1998; Shepherd et al. 1998; Fich & Lada 1997). The model of Matzner & McKee (1999) predicts that the index should indeed be close to 2, with little sensitivity to the environment. Numerical studies of jets are less clear-cut and while it is possible to obtain large indices, they suggest that the environment of the protostar and outflow does play an important role (Downes & Ray 1999).

More recent work by Lee et al. (2001) confirms that jet-driven outflows do tend to have steeper mass-velocity relations ($\gamma \sim 3.5$ can be achieved) than similar wind-driven outflow models ($\gamma \simeq 1.8$). However, their wind-driven models also exhibit another feature observed in many outflows (including G35.2N) and not observed in the jet model: a break in the power law where γ changes from a relatively low value (say 2) increasing to a much steeper value (4 or greater). The presence of a high value for γ as well as a break in the power law may suggest that a wide-angle wind is necessary in addition to a jet. In the models of Lee et al. (2001), the break point occurs at lower velocities for outflows lying closer to the plane of the sky, demonstrating the contraction of the velocity field expected for a predominantly forward-directed flow.

Recently, Arce & Goodman (2001a) have suggested that steep mass-velocity plots can be caused by the superposition of several mass-velocity curves for an episodic outflow. In their picture the individual outbursts have γ=2, in line with the momentum-conserving models of Matzner & McKee (1999), but vary in maximum velocity and amount of mass swept up in each outburst. A similar effect could conceivably result from the superposition of a number of flows with differing properties, such as is the case here in G35.2N. Higher resolution CO observations would allow us to test this as we would be able to resolve the individual outflows and derive their individual mass-velocity indices.

Can the breakdown in our assumptions also explain the observed behaviour? All of our assumptions cause us to underestimate the mass in the flow. The net effect of correcting for all of our main assumptions is to steepen the mass-velocity variation close to the line centre, and flatten it at high velocities, perhaps enough to allow a single power law to fit the data. The effect of correcting for finite optical depth is shown in Table 3 where higher values of γ are derived, a consequence of the fact that the mass will be corrected upwards at low velocities (e.g. Arce & Goodman 2001b). If the excitation temperature increases with velocity then our isothermal assumption will underestimate the mass at high velocities, although this will only a small effect as the population of the J=3 level changes by less than 50 per cent from 33 to 100 K.

If the beam-filling factor of the high-velocity gas decreases with velocity, then correcting for this will also decrease the value of γ. This effect is potentially much larger than either of the previous two (although optical depth effects are important at low velocity). It has some observational support as well in that in a number of outflows the highest-velocity emission does appear to be unresolved (see Fig. 3; also Richer et al. 1992; Gibb & Heaton 1993; Fich & Lada 1997), even in interferometric studies (e.g. Gueth & Guilloteau 1999). Incomplete beam filling may give rise to a break in the mass-velocity spectrum. If we define $v_{\rm fill}$ as the highest velocity at which the emission fills the telescope beam, then for velocities less than $v_{\rm fill}$, we expect that the mass-velocity plot will have a power-law equal to the true value. For velocities greater than $v_{\rm fill}$, the antenna temperature will be reduced, leading to an underestimate of the mass at these velocities and thus causing the mass-velocity plot to fall off more quickly. If the beam-filling factor is a power law of the form $v^{-\alpha_{\rm fill}}$ then a power-law fit to the observed mass-velocity spectrum will have an effective γ given by $\alpha_{\rm fill} + \gamma$. The observed values for γ given in Table 3 suggest that $\alpha_{\rm fill}$ may be as high as 5. It would be useful to know how the filling factor varies for a given beam size in models of outflows. For a sample of similar outflows observed with a beam with FWHM θ, we would expect more distant outflows to have show a break in the m–v plot at smaller velocities. Equivalently we would expect that a sample of flows observed at the same distance would show the same break point, all else being equal (excitation, energetics, inclination). A test of this hypothesis may be through the observations of Ridge & Moore (2001), who did not observe any such correlation.

5.3 Is G35MM2 a high-mass protostar?

From the luminosity and the presence of the radio jet it is clear that the G35.2N core houses massive YSOs (Dent et al. 1985, HL88). Since the envelope appears to be centred on and rotating about G35.2N, it seems likely that it is the most massive object in the group. But what of the other sources, including G35MM2? G35MM2 has no radio source associated with it and is a weaker dust continuum source, indicating a less massive object. Yet its location relative to the CO appears to suggest that it is responsible for a significant portion of the observed CO outflow. Perhaps it represents a lower-mass protostellar object, whose radio emission would be undetectable at 2 kpc. This seems plausible given the weak emission from the G35.2N itself (Table 1). However, G35MM2 is probably not significantly less massive than G35.2N because the mass of the outflowing gas (at least 7 $M_\odot$) seems to rule out a low-mass driving source (e.g. Richer et al. 2000), unless a significant fraction of the outflowing gas arises from another outflow driven by one of the other YSOs in this region.

What does seem likely is that it is more deeply embedded than G35.2N because the ammonia maps of Little et al. (1985) and Brebner et al. (1987) all have clear peaks towards G35MM2, particularly in the case of the (3,3) line (Brebner et al. 1987). In addition our $H^{13}CO^+$ map is skewed towards the position of G35MM2, although the $H^{13}CN$ map is not. (This is most likely due to the $H^{13}CN$ tracing warmer gas towards G35.2N.) The virial mass calculated towards G35MM2 is high at 210 $M_\odot$, which implies a large mean density of 8×10^6 cm^{-3}. The $H^{13}CO^+$ and $H^{13}CN$ and therefore probably tracing a component from the outflow. It seems plausible that G35MM2 may be a massive YSO still in its collapse phase where its H II region is quenched by the action of infalling gas (Walmsley 1995). This is consistent with the scenario where a bipolar outflow is intrinsically linked to active accretion.

Further higher-resolution observations are clearly necessary to determine the properties of G35MM2 and the other sources around G35.2N.

5.4 An organized cluster of massive outflow sources

A simple theory of star formation leads to the conclusion that a rotating envelope which collapses will form a pancake-like core in which new stars emerge with parallel rotation axes perpendicular to the long axis of the core. In practice, such a simple idea

has rarely been observed, and many cores where multiple stars are forming show essentially random orientations of the respective outflow axes both with respect to one another and with respect to the parent core (e.g. Reipurth et al. 1999; Girart et al. 1997). (Note that this problem is not confined to star formation: the direction of jets emanating from the nuclei of Seyfert galaxies shows no correlation with the orientation of the large scale galactic disk: e.g. Kinney et al. 2000; Nagar & Wilson 1999.)

Remarkably, for the most part, the outflows in the G35.2N core *do* seem to have the same alignment; that is north-east to south-west. The intriguing result in the current case is that it is the most luminous source, G35.2N itself, which appears to be discrepant as the axis of the G35MM2 flow is perpendicular to the flattened core. Now the question to answer is why is the radio jet not perpendicular to the long axis of the core, as would normally be expected? Perhaps the formation of the other stars (particularly radio source #6), has exerted a sufficiently large torque to influence the rotation axis of G35.2N. This would suggest that the other sources are indeed high-mass YSOs. Theoretical work on such a scenario is not well developed and so the above description remains rather speculative.

6 CONCLUSIONS: A NEW PICTURE OF G35.2–0.7N

In this paper we have presented a series of observations made with the JCMT, the BIMA millimetre array and the VLA of the massive star-forming region associated with G35.2–0.7N. The combination of these data, along with a reinterpretation of previous observations has led us to develop a new picture for the environment of G35.2N. While superficially the CO 3→2 data support the hypothesis of a jet-driven flow precessing through a large-angle, closer inspection shows that there are probably as many as four outflows associated with the sources in G35.2–0.7N. Much of the structure seen in the CO flow can be explained as at least two overlapping flows. In addition, what was previously believed to be a large-scale, rotating toroid around G35.2N is reinterpreted here as being a rotating flattened, envelope which is fragmented rather than continuous and contains a number of YSOs embedded within dense clumps of gas and dust. VLA observations at 6- and 3.5 cm reveal several embedded YSOs, one of which lies within a previously known ammonia clump.

The presumed most-massive YSO, G35.2N itself, is detected at 3.5 cm and only weakly at 6 cm but appears to be distinguishable by virtue of its positive spectral index and proximity to OH and water masers. The radio jet is resolved into a number of individual knots, whose distribution suggests that the jet is precessing with a half-angle of approximately 10 degrees. Surprisingly, some of the jet knots have positive spectral indices while others have negative values. It is not clear why they should differ so markedly. The northern lobe of the outflow associated with the radio jet has been detected for the first time in CO and possibly SiO. Dust emission from the envelope is detected at 3.5 mm which has a dust-derived mass of 600 to 1400 $M_{\odot}$, depending on the assumed absorption coefficient. The dust emission peaks 3 arcsec south-east of G35.2N, while the $H^{13}CO^{+}$ peaks towards the location of a new millimetre source, G35MM2. G35MM2 marks the position of a deeply embedded massive YSO and is not detected in our VLA images and is most likely the candidate for driving much of the large-scale CO flow.

These results indicate the importance of high-resolution observations in unravelling the processes involved in massive star formation. Even now, higher-resolution dust and molecular line studies are necessary to help further clarify the structure of G35.2–0.7N.

ACKNOWLEDGMENTS:
AGG wishes to thank to Brian Murphy for assistance with the JCMT observations and Greg Taylor at the VLA AOC, Socorro, for help tracking down problems with the VLA data. John Carpenter is thanked for providing data in advance of publication. The referee, Friedrich Wyrowski, is thanked for his comments which helped clarify some points in this paper. AGG acknowledges the financial support of PPARC for a portion of this work. The James Clerk Maxwell Telescope is operated by the Joint Astronomy Centre on behalf of the Particle Physics and Astronomy Research Council of the United Kingdom, the Netherlands Organization for Scientific Research and the National Research Council of Canada. The National Radio Astronomy Observatory is operated by Associated Universities, Inc., under cooperative agreement with the National Science Foundation. BIMA is funded through grant AST-9981289 from the National Science Foundation.

REFERENCES

Allen C.W., 1973, Astrophysical Quantities. Athlone, London.
Anglada G., Villuendas E., Estalella R., Beltrán M.T., Rodríguez L.F., Torrelles J.M., Curiel S., 1998, AJ, 116, 2953
Arce H.G., Goodman A.A., 2001a, ApJ, 551, L171
Arce H.G., Goodman A.A., 2001b, ApJ, 554, 132
Bachiller R., Guilooteau S., Gueth F., Tafalla M., Dutrey A., Codella C., Castets A., 1998, A&A, 339, L49
Bally J., Lada C.J., 1983, ApJ, 265, 824
Beuther H., Schilke P., Sridharan T.K., Menten K.M., Walmsley C.M., Wyrowsk F., 2002, A&A, 383, 892
Bonnell I.A., Bate M.R., Clarke C.J., Pringle J.E., 1997, MNRAS, 285, 201
Brebner G.C., Cohen M.J., Heaton B.D., Davies S.R., 1987, MNRAS, 229, 679
Claussen M.J., Marvel K.B., Wootten A., Wilking B.A., 1998, ApJ, 507. L79
Cliffe J.A., Frank A., Jones T.W., 1996, MNRAS, 282, 1114
Codella C., Bachiller R., Reipurth B., 1999, A&A, 343, 585
Davis C.J., Moriarty-Schieven G.M., Eislöffel J., Hoare M.G., Ray T.P., 1998, AJ, 115, 1118
Dent W.R.F., Little L.T., White G.J., 1984, MNRAS, 210, 173
Dent W.R.F., Little L.T., Kaifu N., Ohishi M., Suzuki S., 1985, A&A, 146, 375
Dent W.R.F., Little L.T., Sato S., Ohishi M., Yamashita T., A&A, 217, 217
Dent W.R.F., Sandell G., Duncan W.D., Robson E.I., 1989, MNRAS, 238, 1497
Downes T.P., Ray T.P., 1999, A&A, 345, 977
Eislöffel J., 1997, in Reipurth B., Bertout C., eds, Herbig-Haro Flows and the Birth of Low Mass Stars. Kluwer, Dordrecht, p.93
Fich M., Lada C.J., 1997, ApJ, 484, L63
Forster J.R., Caswell J.L, 1999, A&AS, 137, 43
Fuller G.A., Zijlstra A.A., Williams S.J., 2001, ApJ, 555, L125
Ghavamian P., Hartigan P., 1998, ApJ, 501, 687
Gibb A.G., Davis C.J., 1998, MNRAS, 298, 644
Gibb A.G., Heaton B.D., 1993, A&A, 276, 511
Girart J.M., Estalella R., Anglada G., Ho P.T.P., Rodríguez L.F., 1997, ApJ, 489, 734
Goldreich P., Kwan J., 1974, ApJ, 189, 441
Gueth F., Guilloteau S., 1999, A&A, 343, 571
Heaton B.D., Little L.T., 1988, A&A, 195, 193
Henriksen R., Ptuskin V.S., Mirabel I.F., 1991, A&A, 248, 221
Hoare M.G., 2002, in Crowther P.A., ed, The Earliest Phases of Massive Star Birth. San Francisco, The Astronomical Society of the Pacific, p.137

Hoare M.G., Drew J.E., Muxlow T.B., Davis R.J., 1994, ApJ, 421, L51
Hollenbach D.J., McKee C.F., 1979, ApJS, 41, 555
Hutawarakorn B., Cohen R.J., 1999, MNRAS, 303, 845
Irvine W.M., Goldsmith P.F., Hjalmarson Å, 1987, in Hollenbach D.J., Thronson H.A., Jr, eds, Interstellar Processes. Reidel, Dordrecht, p. 561
Kinney A.L., Schmitt H.R., Clarke C.J., Pringle J.E., Ulvestad J.S., Antonucci R.R.J., 2000, ApJ, 537, 152
Lada C.J., 1985, ARA&A, 23, 267
Lada C.J., Fich M., 1996, ApJ, 459, 638
Lee C-F., Mundy L.G., Reipurth B., Ostriker E.C., Stone J.M., 2000, ApJ, 542, 925
Lee C-F., Stone J.M., Ostriker E.C., Mundy L.G., 2001, ApJ, 557, 429
Little L.T., Dent W.R.F., Heaton B.D., Davies S.R., White G.J., 1985, MNRAS, 217, 227
Little L.T., Kelly M.L., Murphy B.T., 1998, MNRAS, 294, 105
Martí J., Rodríguez L.F., Reipurth B., 1993, ApJ, 416, 208
Masson C.R., Chernin L.M., 1992, ApJ, 387, L47
Matzner C.D., McKee C.F., 1999, ApJ, 526, L109
Mezger P.G., Chini R., Kreysa E., Wink J., 1987, A&A, 182, 127
Nagar N.M., Wilson A.S., 1999, ApJ, 516, 97
Panagia N., Felli M., 1975, A&A, 39, 1
Reipurth B., Yu K.C., Rodríguez L.F., Heathcote S., Bally J., 1999, A&A, 352, L83
Richer J.S., Hills R.E., Padman R., 1992, MNRAS, 254, 525
Richer J.S., Shepherd D.S., Cabrit S., Bachiller R., Churchwell E., 2000, in Mannings V., Boss A.P., Russell S.S., eds, Protostars & Planets IV. University of Arizona Press, Tucson, p.867
Rodríguez L.F., 1997, in Reipurth B., Bertout C., eds, Herbig-Haro Flows and the Birth of Low Mass Stars. Kluwer, Dordrecht, p.83
Schilke P., Walmsley C.M., Pineau des Forêts G., Flower D.R., 1997, A&A, 321, 293
Shepherd D.S., Watson A.M., Sargent A.I., Churchwell E., 1998, ApJ, 507, 861
Shepherd D.S., Yu K.C., Bally J., Testi L., 2000, ApJ, 535, 833
Simon M., Felli M., Massi M., Cassar L., Fischer J., 1983, ApJ, 266, 623
Torrelles J.M., Gómex J.F., Rodríguez L.F., Curiel S., Ho P.T.P., Garay G., 1996, ApJ, 457, L107
Vallée J.P., Bastien P., 2000, ApJ, 530, 806
Walther D.M., Aspin C.A., McLean I.S., 1990, ApJ, 356, 544
Wilner D.J., Reid M.J., Menten K.M., 1999, ApJ, 513, 775
Wright A.E., Barlow M.J., 1974, MNRAS, 170, 41

This paper has been typeset from a TEX/ LATEX file prepared by the author.